Research Article

Received: 1 December 2025 Revised: 19 March 2026 Published online in Wiley Online Library: 28 April 2026

(wileyonlinelibrary.com) DOI 10.1002/ps.70860

A geometric and probabilistic framework for mechanistic antifungal screening from colony morphology

Ezekiel Ahn,[a*] Insuck Baek,[b] Seunghyun Lim,[a] Amelia Lovelace,[a] Masoud Kazem-Rostami,[c] Helen Ngo,[c] Richard D Ashby,[c] Minhyeok Cha,[b] Moon S Kim,[b] Sunchung Park[a] and Lyndel W Meinhardt[a]

Abstract

BACKGROUND: Fungicide discovery still relies heavily on scalar screening endpoints [e.g. inhibition zones, median effective concentration (EC_{50}) or minimum inhibitory concentration (MIC)] that summarize growth suppression but provide limited information about geometry-linked failure modes, constraining mechanistic prioritization during early screening. Because colony morphology encodes growth direction and polarity, we developed a geometric and probabilistic screening framework to separate potency from polarity-linked failure modes in cacao- and coffee-relevant pathogens.

RESULTS: From routine colony images, we computed a fixed-dose potency coordinate, λ, as the negative natural log of the area survival ratio, and a polarity coordinate, *I*, as the natural log fold-change in length-to-width ratio (treated/control). We then estimated polarity-disruption event probability ($\hat{p}$) with exact 95% Clopper–Pearson confidence bounds at an operational threshold of $\tau = 1.10$, with sensitivity analysis across $\tau = 1.10$–1.20. In a single-dose primary screen across nine isolates and four phenolic-branched amide/acid candidates, amides consistently clustered in the ($+\lambda$, $+I$) quadrant, indicating an action direction characterized by concurrent growth suppression and polarity disruption relative to the acid analogues. The strongest combination was CGH5 treated with PhSOAM ($\lambda = 0.67$), which also showed high shape-disruption probability ($\hat{p} = 0.75$; 95% CI 0.43–0.95). Ellipse-based axis reconstruction linked *I* to axis-specific contraction ratios and showed strong agreement with direct length- and width-based ratios. Re-analysis of an independent UV-C exposure-time gradient (0–30 min) produced coherent dose-dependent $\lambda(d)$ and $I(d)$ trajectories and supported event-level inference at ~10 min.

CONCLUSION: The λ–*I*–*p* grammar converts colony images into an instrument-agnostic screening language describing how strongly an intervention acts at the tested condition (λ), whether it is associated with polarity-linked geometry change (*I*) and how often a defined failure mode occurs ($\hat{p}$), thereby supporting mechanistic screening and prioritization of candidate fungicides.
Published 2026. This article is a U.S. Government work and is in the public domain in the USA.

Supporting information may be found in the online version of this article.

Keywords: anisotropy; antifungal mode-of-action; crop protection; event-level statistics; fungicide screening; image-based assay; morphology-based phenotyping

1 INTRODUCTION

Fungicides remain a cornerstone of crop protection, yet resistance is eroding the efficacy of many existing active ingredients, and the pipeline for new products is under pressure.[1–3] In this setting, discovery programmes increasingly need tools that do more than rank candidates by overall growth inhibition. They must also reveal how a treatment damages the fungus, so that compounds with genuinely novel modes-of-action (MoAs) can be prioritized for further development and resistance-management strategies. However, most *in vitro* assays still summarize responses using scalar metrics such as inhibition zones, minimum inhibitory concentrations (MICs) or median effective concentration (EC_{50}) values.[4–6] These endpoints are useful for comparing potency, but they provide limited resolution for distinguishing geometry-linked response patterns or for prioritizing compounds that may differ mechanistically despite similar scalar potency.

* *Correspondence to: E Ahn, Sustainable Perennial Crops Laboratory, Agricultural Research Service, United States, Department of Agriculture, Beltsville, MD, 20705, USA. E-mail: ezekiel.ahn@usda.gov*

a *Sustainable Perennial Crops Laboratory, Agricultural Research Service, United States, Department of Agriculture, Beltsville, MD, USA*

b *Environmental Microbial and Food Safety Laboratory, Agricultural Research Service, United States, Department of Agriculture, Beltsville, MD, USA*

c *Sustainable Biofuels and Co-Products Research Unit, Agricultural Research Service, United States Department of Agriculture, Eastern Regional Research Center, Wyndmoor, PA, USA*

Colony images already contain the information needed to bridge this gap. Mycelial morphology integrates the effects of genotype, environment and chemical stress, and changes in polarity and growth direction are tightly linked to fundamental processes such as cell-wall biosynthesis and hyphal tip growth.[7–10] This has motivated a shift toward high-content, image-based phenotypic screening in filamentous fungi.[11–14] Yet the field still lacks a compact quantitative representation, a 'grammar,' that unifies colony size and shape into comparable mechanistic coordinates that can be applied across isolates and, in principle, across stress modalities. In particular, current pipelines report how much growth is suppressed but rarely quantify whether colonies fail isotropically or along a preferred axis, even though this distinction is central to MoA.

Here we introduce a compact grammar with three components. First, we define a potency coordinate $\lambda_{area} = -\ln(S_{area})$, the negative log of the area survival ratio, which places treated groups on a linear scale where equal steps correspond to equal multiplicative changes in suppression. Second, we define polarity $l_{LWR} = \ln(LWR_t/LWR_c)$, a size-normalized contrast that tracks shifts in colony anisotropy. Together, these form a MoA vector $v = (\lambda_{area}, l_{LWR})$ with an angle θ (action direction) and a magnitude $|v|$ (combined effect size). Third, we convert morphology from means into event-level claims by estimating $p(LWR \geq \tau)$ with exact binomial confidence bounds,[15] so that statements about polarity disruption are frequency-based and reproducible rather than anecdotal. For cross-modal datasets (e.g. UV-C), events are equivalently defined on the polarity coordinate $[l \geq \ln(\tau)]$, ensuring mathematical consistency across modalities. This morphology-based λ–l–p grammar is designed to integrate seamlessly into fungicide screening workflows, providing crop-protection programmes with mechanistic, QC-ready endpoints that complement conventional potency-only screening.

Applied to a panel of isolates and four related chemistries (amide/acid pairs), this framework yields three findings that a scalar pipeline would miss. (i) Amide treatments do not merely rank higher on potency; they cluster in the (+potency, +polarity) quadrant, revealing an action direction, polarity-disruptive suppression, distinct from acids. (ii) Reconstructing major and minor axes from area and LWR shows bidirectional axis contraction, linking the polarity signal to a concrete geometric failure (narrowing outpaces shortening). (iii) At a predefined threshold (e.g. $\tau = 1.10$), the incidence of polarity-disruption events is high in amides, whereas controls remain lower than the strongest treated groups, and sensitivity analyses ($\tau = 1.10 - 1.20$) showed that the main treatment–control contrasts remained interpretable across stricter operational thresholds.

Conceptually, this potency–polarity–probability triad elevates morphology from description to explanation. It enables ranking by how much a treatment works (λ), grouping by how it works (θ), and certifying how often it works (p_τ), a combination that aligns with both discovery decisions and mechanistic follow-up. Because the ingredients are generic (areas, LWRs, replicate counts), the approach is instrument-agnostic and pathosystem-agnostic: the exact coordinates can be used to compare chemical,[16] photonic (UV-C)[17,18] or biocontrol modalities[19,20] on a common mechanism map. Additionally, we demonstrate this cross-modal portability herein by re-analyzing the UV-C dose–response data, proving the $\lambda - l - p$ grammar holds for both chemical and physical stressors. Accordingly, our objective was to establish and evaluate a colony-morphology framework that separates potency from polarity-linked geometry change and expresses replicate-level event frequency with exact confidence bounds in a fixed-dose chemical screen, while testing whether the same grammar remains coherent under an independent UV-C dose gradient. In this sense, turning morphology into vectors, angles and event bounds is not ornamentation on top of potency; it is a necessary quantitative language for understanding how antifungals act in early screening contexts.

2 MATERIALS AND METHODS

2.1 Dataset and source data

All data processing, metric calculations and statistical analyses were performed in Python (v3.11) using the pandas,[21] numpy[22] and scipy[23] libraries. All analyses were based on a pre-existing, replicated dataset derived from *in vitro* cultures of nine fungal isolates. These included six coffee-pathogenic isolates of *Colletotrichum* spp. (P23-55, P24-83, P24-85, P24-88, P24-192 and P24-193), which were originally isolated from *Coffea arabica* plants in various regions in Hawaii, and three cacao-pathogenic isolates: *Pestalotiopsis* sp. CGH5, and *Colletotrichum gloeosporioides* CGH17 and CGH49, sourced from *Theobroma cacao* in Ghana. These pathogens are known to cause significant diseases in their respective hosts, such as anthracnose in coffee and cacao, leading to substantial agricultural losses.[24,25]

The isolates were tested against four novel phenolic-branched compounds derived from sustainable feedstocks: phenolic soybean oil branched fatty amide (PhSOAM) and its corresponding acid form (PhSOFA), as well as beechwood creosote-branched brown grease fatty amide (BCBGAM) and its acid form (BCBGFA). These compounds were produced and characterized as detailed in prior reports,[24,26–28] with the amide derivatives featuring ethylenediamine-carrying modifications to enhance stability and antifungal activity. Each compound was dissolved in pure ethanol to create stock solutions of 10 mg mL^{-1} before application, alongside an untreated (ethanol-only) control. The dataset captures quantitative morphological responses from these *in vitro* assays, enabling the geometric and probabilistic mapping of antifungal action as described in the manuscript.

Chemical screening was designed as a single fixed-dose primary screen (with a matched vehicle control) to enable standardized mechanistic comparison across chemistries without introducing additional assumptions from dose selection and curve-fitting. Accordingly, the present study does not aim to report chemical EC_{50} values; instead, it establishes a portable λ–l–p coordinate system computed from unitless treated-to-control ratios at the screening dose. Dose-dependent trajectories are explicitly demonstrated in the independent UV-C exposure-time gradient analysis, showing that the same λ–l–p definitions apply pointwise in dose–response settings.

2.2 Quantification of morphological metrics

2.2.1 *Potency (λ) and polarity (l) definition*

In order to linearize and standardize comparisons, we first computed the survival ratio (S_k) for a given metric k as the ratio of the treated mean to the control mean:

$$S_k = \frac{\overline{X}_{k,\text{treated}}}{\overline{X}_{k,\text{control}}}$$

Potency (λ), representing growth suppression, was defined as the negative natural log of the area survival ratio (S_{area}). This

Published 2026. This article is a U.S. Government work and is in the public domain in the USA.

log-transform places suppression on an additive, linear scale where 0 indicates no effect:

$$\lambda_{area} = -\ln(S_{area})$$

Polarity (I), a size-normalized measure of shape anisotropy, was defined as the log-fold-change of the length-to-width ratio (LWR). This log-ratio transform centers the comparison at 0 (no change in shape) and makes increases and decreases interpretable on a symmetric scale:

$$I_{LWR} = \ln\left(\frac{\overline{LWR}_{treated}}{\overline{LWR}_{control}}\right)$$

2.2.2 Mode-of-action vectorization

These two orthogonal metrics, λ_{area} and I_{LWR}, were used to define a 2D MoA vector $v=(\lambda_{area}, I_{LWR})$ for each isolate-compound pair. The vector's magnitude, $|v|=\sqrt{\lambda_{area}^2+I_{LWR}^2}$, quantifies the overall effect size. The vector's angle, $\theta=\text{atan2}(I_{LWR}, \lambda_{area})$, defines the action direction, distinguishing between pure potency ($I\approx 0$) and polarity disruption ($I>0$).

2.2.3 Axis-specific ratio reconstruction

In order to infer underlying geometric changes, we modelled the colony as an ellipse where Area $A\propto a\cdot b$ (major axis a, minor axis b) and LWR$=a/b$. Based on this assumption, the ratios of the treated *versus* control axes (a_t/a_c and b_t/b_c) were algebraically derived from the two primary metrics (S_{area} and S_{LWR}) as follows:

$$\frac{a_t}{a_c} = \sqrt{S_{area}\cdot S_{LWR}}$$

$$\frac{b_t}{b_c} = \sqrt{S_{area}/S_{LWR}}$$

where $S_{LWR}=\overline{LWR}_{treated}/\overline{LWR}_{control}$. These ratios were used to assess physical contraction along each axis. We constructed the core λ–I grammar from two morphology outputs that are routinely available across platforms (area and LWR), enabling low-barrier adoption without requiring additional assays. The framework is modular: other quantitative phenotypes (e.g. branching indices, sporulation counts, enzyme activity readouts) can be incorporated as additional coordinates or event definitions whenever such measurements are available, using the same treated-to-control ratio logic and replicate-level counting for probabilistic statements. Because this reconstruction uses an ellipse approximation, the derived axis ratios should be interpreted as screening-level geometric surrogates rather than exact physical measurements for highly irregular colonies. To evaluate whether this simplification preserved the dominant geometry signal in the present dataset, we compared reconstructed axis ratios against direct length- and width-based ratios computed from the same isolate-treatment summaries (Supporting Information, Fig. S1).

2.3 Probabilistic framework for event analysis

In order to move beyond mean-based comparisons, we operationalized a 'polarity disruption event' at the individual colony level, defined, for the main chemical screen, as LWR $\geq \tau$, where τ is a predefined operational threshold. The probability of this event, p, was estimated as the observed frequency $\hat{p}=k/n$ (where k events were observed in n replicates).

In order to provide rigorous statistical guarantees, we computed the exact 95% confidence interval (CI) for p using the Clopper–Pearson 'exact' method.[15] This method was specifically chosen as it is robust for small sample sizes (n) and for probabilities near 0 or 1, which are common in control groups. The primary threshold $\tau = 1.10$ was used as a practical decision rule representing a modest but directional departure from control-like colony shape, whereas additional thresholds ($\tau = 1.15$ and 1.20) were evaluated to determine whether the main treatment–control contrasts were robust to stricter event definitions.

Sensitivity analyses were performed using three distinct thresholds: $\tau = 1.10, 1.15$ and 1.20. To assess the dependence of event frequency on threshold choice, we summarized matched treated and control probabilities across $\tau = 1.10$, 1.15 and 1.20, enabling direct visual comparison of threshold sensitivity (Fig. S2). This sensitivity analysis was used to verify whether the main treatment–control contrasts remained interpretable under stricter event definitions.

2.4 Cross-modal validation using a physical stressor (UV-C) dataset

In order to demonstrate portability across stress modalities, we reanalyzed a published UV-C dose–response dataset involving cacao isolates (CGH5, CGH17, CGH34, CGH38, CGH53) and coffee isolates (P23-55, P24-83, P24-85, P24-88, P24-193).[17,29] For this dataset, dose (d) was defined as exposure time (min). Because the UV-C dataset provides a continuous gradient (0–30 min), we computed $\lambda(d)$ and $I(d)$ pointwise at each dose, enabling the visualization of dose-dependent trajectories. This UV-C dataset therefore serves as an external dose-gradient validation of the λ–I–p grammar without requiring additional chemical dose–response experiments. For event probability $p(d)$, events were defined on the polarity coordinate ($I \geq \ln\tau$), which is algebraically consistent with thresholding LWR in log-ratio space.

2.5 Practical implementation and resource requirements

Practical implementation requirements, outputs, and computational efforts compared to conventional potency-only screening are summarized in Table 1.

3 RESULTS

3.1 A morphology-based coordinate system for fungicide potency and mode-of-action

In order to complement conventional potency-only metrics, we developed a framework to quantify antifungal responses using two mechanistically informative coordinates: potency (growth suppression) and polarity (shape disruption).

First, we mapped the potency landscape by calculating λ_{area} (the negative log-transform of the area survival ratio). The resulting heatmap (Fig. 1) reveals significant isolate-dependent heterogeneity and highlights the superior potency of amide formulations. λ_{area} values spanned from −0.15 (slight growth promotion) to a maximum of 0.67 at the CGH5–PhSOAM combination, corresponding to an area survival of $S_{area}\approx 0.51$ (a 49% reduction relative to control). By contrast, the acid analogue PhSOFA on the same isolate showed a much weaker potency ($\lambda = 0.38$).

Second, to decouple this potency from shape-based mechanisms, we projected each treatment pair into a MOA vector plane

Published 2026. This article is a U.S. Government work and is in the public domain in the USA.

Table 1. Practical inputs, outputs and implementation effort of potency-only screening *versus* the λ–I–p framework

Aspect	Conventional potency-only screen	λ–I–p framework
Primary experimental input	Colony imaging + area (growth) measurement; treated *vs* control	Same imaging; re-uses area plus simple anisotropy descriptor (LWR) from the same images
Potency readout	Area survival ratio or % inhibition (often reported at a fixed time/dose)	$\lambda = -\ln(S_{area})$ (monotonic transform of area survival; preserves potency ranking)
Geometry / mechanistic separation	Not quantified (potency-only collapses different shape responses)	$I = \ln(LWR_t/LWR_c)$ separates polarity/anisotropy effects at matched potency
Axis-specific reconstruction	Not available	Ellipse-model reconstruction: $a_{ratio} = \sqrt{S_{area} \cdot e^I}$, $b_{ratio} = \sqrt{S_{area}/e^I}$
Event-level inference	Typically not reported (or reported without formal uncertainty bounds)	$\hat{p}$ = Pr(event) with exact 95% Clopper–Pearson CI across replicate colonies; sensitivity across τ.
Cross-modal transfer / dose trajectories	No standard way to compare across modalities	Identical grammar applied pointwise to dose/time gradients: $\lambda(d)$, $I(d)$, $p(d)$ (UV-C validation)
Added wet-lab cost	—	None (analysis-only; no additional assays required)
Added analysis burden	Basic spreadsheet summary	Provided scripts produce Data S1 (full reproducibility)

Note: The λ–I–p framework requires no additional experimental assays beyond standard colony imaging; it re-uses routine image-derived features (area and LWR) and replicate counting to provide potency (λ), polarity (I) and event probability with exact confidence bounds (p).

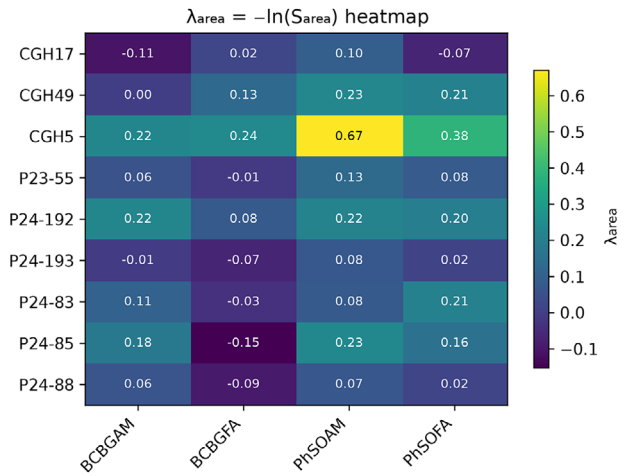

Figure 1. Potency map ($\lambda_{area} = -\ln S_{area}$). Heatmap of potency ($\lambda_{area}$) over isolates and compounds. Values range from −0.15 to 0.67, with the maximum potency (darkest red) observed at CGH5–PhSOAM = 0.67 ($S_{area} \approx 0.51$). Acid analogues generally show smaller λ values, and occasional negative values (e.g. P24-85–BCBGFA = −0.15) indicate slight overgrowth relative to control.

(λ_{area}, I_{LWR}), where I_{LWR} quantifies the log-ratio change in the LWR (Fig. 2). This vector field clearly shows that most treatment vectors, particularly the amides (PhSOAM/BCBGAM), occupy the (+λ, +I) quadrant. This indicates concurrent growth suppression (λ>0) and polarity disruption (I_{LWR}>0), visually separating them from their acid counterparts, which clustered closer to the x-axis (potency-only).

Importantly, because λ is defined as $\lambda = -\ln(S_{area})$, it is a monotonic transform of the standard area-based inhibition readout and therefore preserves the same treatment ranking as conventional potency-only screening. The added coordinates I and p, however, provide mechanistic and reproducibility information that potency alone cannot: for example, two treatments can exhibit similar λ yet diverge in I, indicating distinct geometry-altering effects. We highlight representative examples in the main text and summarize additional cases in Table S1. This added resolution enables mechanistic triage at the primary-screen stage without requiring new assays. For example, on isolate CGH49, PhSOAM and PhSOFA show similar potency ($\lambda = 0.226$ *versus* 0.208) but markedly different polarity ($I = 0.121$ *versus* 0.032), which would be treated as 'similar' under potency-only screening yet clearly diverges under the λ–I map.

3.2 Cross-modal validation shows that the λ–I–p grammar is portable from fungicides to UV-C stress

We next tested if our $\lambda - I - p$ grammar could be generalized from chemical stressors to physical stressors using a published UV-C dataset.[17] The analysis demonstrates that our framework is portable. Potency (λ) increased clearly in a dose-dependent manner with UV-C exposure time [Fig. 3(a)]. Polarity (I_{LWR}), the metric of 'how' the fungus fails, also exhibited consistent, nonzero dose-dependent shifts [Fig. 3(b)]. Finally, the probabilistic event framework was validated using the Coffee ~10 min cohort by estimating the probability of a shape-disruption event ($I \geq \ln \tau$, $\tau = 1.10$) and its exact 95% Clopper–Pearson confidence bounds [Fig. 3(c)]. This confirms that our framework successfully maps 'how much' (λ), 'how' (I) and 'how often' (p^) for both chemical and physical modalities, demonstrating that the λ–I–p grammar is portable across stress types. Note that, for the chemical screen, we operationalized events on the absolute LWR scale (LWR ≥ τ), whereas for the UV-C dataset, we defined events directly on I ($I \geq \ln \tau$); because I is the log-ratio of LWR, these two definitions quantify the same underlying polarity-disruption phenomenon in algebraically linked coordinates.

3.3 Geometric reconstruction links polarity disruption to physical axis contraction

In order to understand the physical meaning of the I_{LWR} (polarity) signal, we reconstructed the individual major (a_t/a_c) and minor (b_t/b_c) axis ratios. This decomposition confirmed that the observed polarity shift corresponds to a tangible geometric failure mode (Fig. 4). For representative isolates (e.g. P24-193), amides induced bidirectional suppression, with both axis ratios falling below 1.0, linking the positive I_{LWR} signal to a cooperative

Published 2026. This article is a U.S. Government work and is in the public domain in the USA.

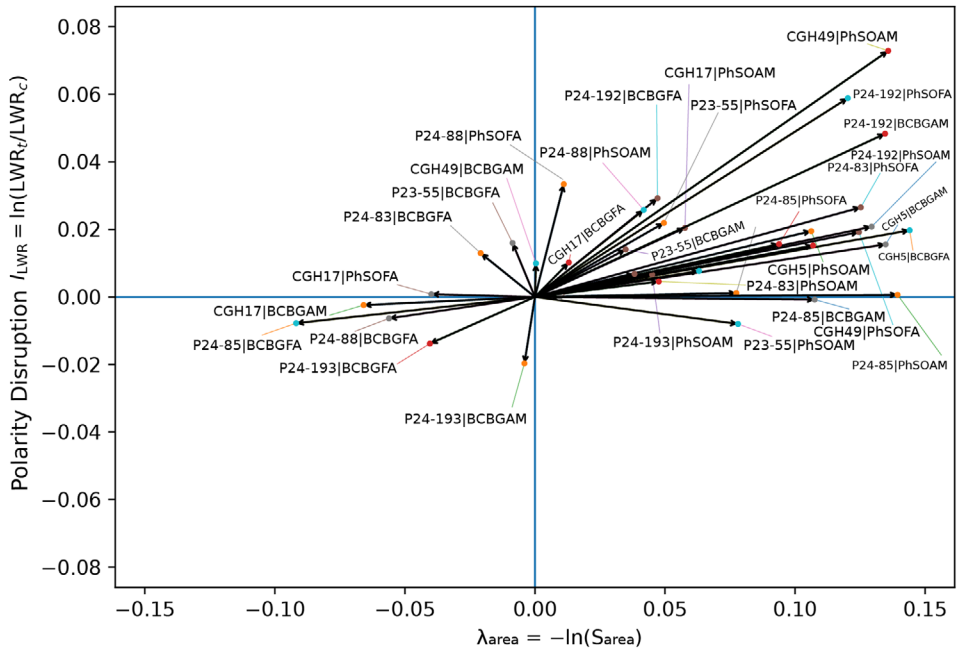

Figure 2. MoA vector field (potency versus polarity). Each arrow originates at (0,0) and points to (λ_{area}, l_{LWR}) for an isolate-compound pair. λ_{area} (x-axis) quantifies potency, while l_{LWR} (y-axis) quantifies shape anisotropy (polarity disruption). The consistent clustering of amide treatments in the first quadrant ($+\lambda$, $+l$) indicates a distinct mechanism defined by concurrent potency and polarity disruption.

suppression of colony geometry. The reconstructed major- and minor-axis ratios across all isolate–treatment pairs are provided in Fig. S3. Although the axis ratios were derived under an ellipse model, the reconstructed values closely matched direct length- and width-based ratios across isolate-treatment summaries ($r = 0.993$ for the major axis and $r = 0.997$ for the minor axis; Fig. S1), supporting the use of the reconstruction as a compact surrogate for axis-specific geometry in this screening context.

3.4 Event-level bounds provide probabilistic endpoints for antifungal screening

Finally, to translate mean-level effects into reproducible claims, we operationalized polarity disruption as a discrete 'event' $[p(\mathrm{LWR} \geq \tau))]$ and calculated its probability with exact 95% Clopper–Pearson confidence bounds. The complete list of replicate counts (n), event counts (k), estimated probabilities ($\hat{p}$), and exact 95% CIs for all thresholds is provided in Data S1. At the primary threshold $\tau = 1.10$ (Fig. 5), PhSOAM yielded high event probabilities in multiple isolates, including CGH5 ($\hat{p} = 0.75$), P24-88 ($\hat{p} = 0.70$) and CGH49 ($\hat{p} = 0.58$), whereas vehicle-only controls remained lower than the strongest PhSOAM-treated groups (control probabilities at $\tau = 1.10$ were generally 0.00–0.25 and decreased further under stricter thresholds; Data S1). The main pattern was not restricted to a single operational cutoff. When the event threshold was varied from $\tau = 1.10$ to 1.15 and 1.20, absolute probabilities decreased as expected under stricter criteria, whereas the main treatment–control contrasts remained visible for the strongest combinations (Fig. S2).

Together, the maximal potency ($\lambda = 0.67$ at CGH5–PhSOAM) (Fig. 1), the MoA vector pattern (Fig. 2), the physical axis contractions (Fig. 4) and the high event-probability gaps at $\tau = 1.10$ (Fig. 5) collectively indicate that amide chemistries, especially PhSOAM, produce stronger growth suppression coupled with reproducible, geometrically-defined polarity disruption across diverse isolates.

4 DISCUSSION

This work introduces a new way to quantify and interpret antifungal responses from colony morphology. For decades, the field has relied on scalar metrics such as EC_{50} or MIC, which summarize potency in a single number.[1] Although these endpoints are useful, they do not explicitly capture the geometry-linked response patterns analyzed here.[2] Our study complements this scalar view with a multidimensional grammar composed of three components: potency (λ), polarity-linked direction (l) and event probability (p).

By projecting antifungal treatments into this coordinate system, we separate how strongly a treatment acts at the tested condition from whether it is associated with directional geometry change. Importantly, this grammar is not limited to the present chemical screen. By re-analyzing a published UV-C dataset,[17] we showed that the λ–l–p framework also captures dose-dependent potency $\lambda(d)$, polarity shifts $l(d)$ and probabilistic failure events $p(d)$ under an independent physical stressor [Fig. 3(A)–(C)]. This cross-modal coherence supports the framework's use as a portable screening language.

4.1 The MoA vector field: a new map for antifungal mechanisms

The potency heatmap (Fig. 1) confirms the value of λ_{area} as a robust potency coordinate for ranking antifungal strength at the tested condition, revealing PhSOAM as a highly potent treatment for specific isolates (for example, $\lambda = 0.67$ for CGH5). However, this map alone does not explain why a treatment is potent. That information resides in the MoA vector field (Fig. 2), which serves as the centerpiece of our framework.

This map reveals a clear qualitative separation between chemical classes. Amide treatments (PhSOAM, BCBGAM) consistently cluster in the ($+\lambda$, $+l$) quadrant, defined by concurrent potency ($\lambda > 0$) and polarity disruption ($l_{LWR} > 0$). By contrast, their acid counterparts (PhSOFA, BCBGFA) cluster near the x-axis, exhibiting potency but lacking a consistent polarity signal. This is an

Published 2026. This article is a U.S. Government work and is in the public domain in the USA.

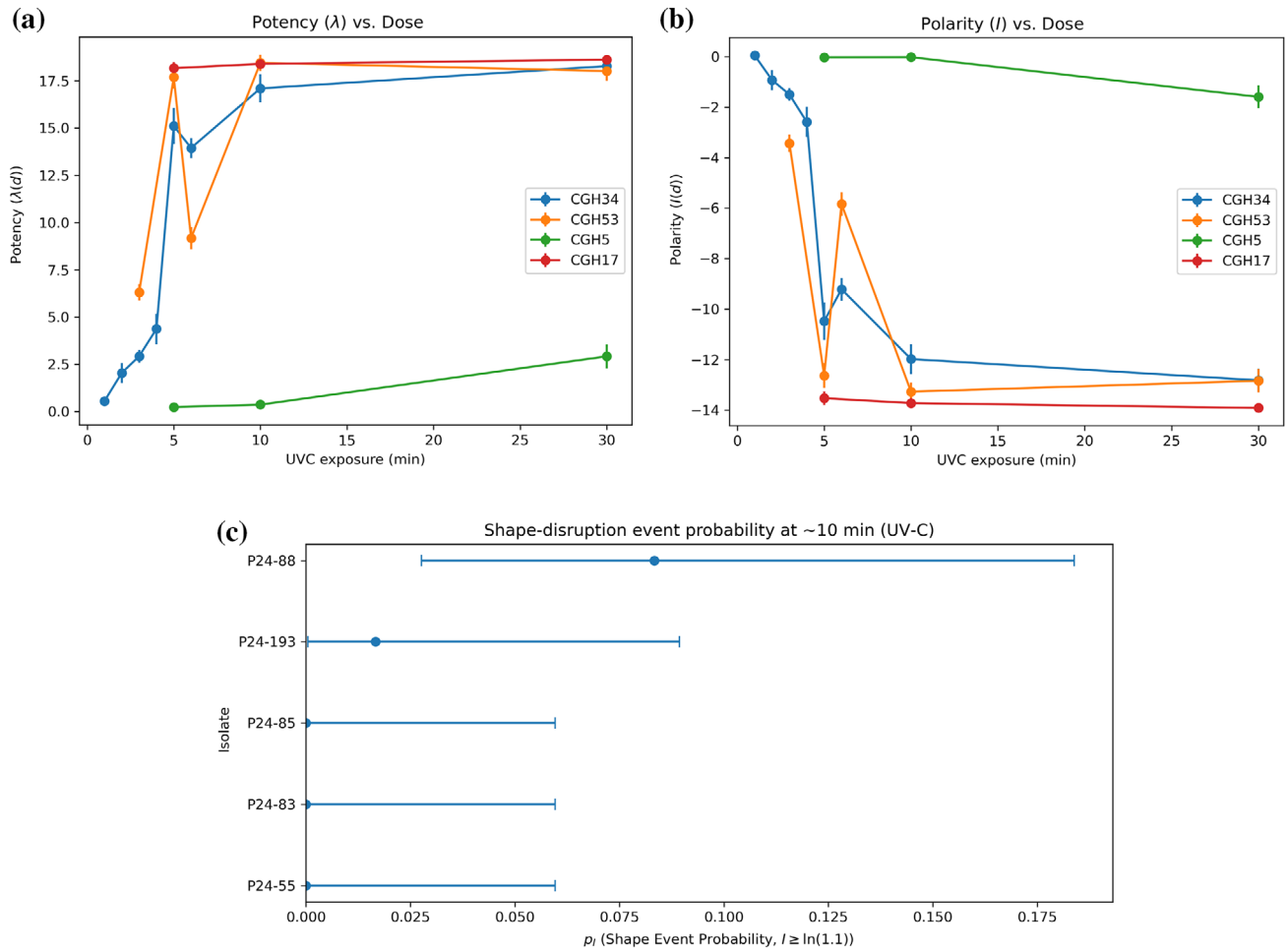

Figure 3. Cross-modal validation of the $\lambda - I - p$ grammar using a re-analyzed UV-C dataset. (a) Potency [$\lambda(d)$] increases with UV-C exposure time (in min) for Cacao isolates. (b) Polarity [$I(\mathrm{d})$] shows corresponding dose-dependent shifts. (c) Event-level bounds for shape disruption $\widehat{p}_I \pm 95\,\%$ CI at $I \geq ln(1.10)$ in Coffee isolates at ~10 min UV-C.

important finding: amides are not only stronger than acids in several isolate backgrounds, but also occupy a different region of the λ–I plane. This aligns with structure–activity relationship (SAR) studies showing that converting acids to amides can dramatically alter bioactivity.[30,31] Our findings, interpreted alongside prior work on phenolic-branched fatty amides and related derivatives,[24,26–28] suggest that this modification is associated with a 'polarity-disruptive' (high-I) phenotypic component.

This framework provides a quantitative tool for SAR-orientated comparison based on action direction as well as potency, allowing compounds to be grouped in the λ–I plane rather than evaluated by potency alone. From a crop-protection perspective, this map therefore functions as a screening tool rather than a purely descriptive construct. Compounds that fall into distinct regions of the λ–I plane represent candidates with potentially novel or under-exploited MoAs, even when their scalar potency is similar. In particular, the consistent placement of amide chemistries in the 'polarity-disruptive' quadrant indicates that their activity is not fully summarized by potency alone, which is relevant for resistance-management contexts that seek chemically distinct response patterns.

4.2 From abstract signal to physical reality

The 'polarity' signal ($I_{LWR}>0$) is not merely a statistical abstraction. Our axis-specific reconstruction (Fig. 4) provides its physical validation. It indicates that a positive I_{LWR} (increased elongation) is not a result of the colony growing longer, but rather a bidirectional axis contraction where the minor axis (b_t/b_c) contracts more severely than the major axis (a_t/a_c). This concept of linking quantitative metrics to physical geometry is supported by biomechanical models of hyphal tip growth[8] and colony pressure profiling.[32] Our $\lambda - I$ map provides a high-throughput readout for this geometric failure mode, linking the abstract I_{LWR} coordinate to a testable physical 'pinching' phenotype associated with amide treatment in this dataset.

Furthermore, the probabilistic event analysis (Fig. 5) provides quantitative support that this failure mode is reproducible at the replicate level. By showing that $p(\mathrm{LWR} \geq 1.10)$ is high for PhSOAM (e.g. $\hat{p} \approx 0.75$ for CGH5, $\hat{p} \approx 0.70$ for P24-88 and $\hat{p} \approx 0.58$ for CGH49) while remaining lower in matched controls, we show that this pattern is not driven by a few extreme outliers but is detectable at the population level. This shifts the interpretation from simple significance testing toward explicit replicate-level event frequencies with exact confidence intervals, yielding a more transparent and reproducible description of failure incidence. The ellipse-model reconstruction is intentionally a low-parameter approximation, not a full contour-recovery model. However, its strong agreement with direct length- and width-based ratios in the present dataset (Fig. S1) indicates that the inferred axis

Published 2026. This article is a U.S. Government work and is in the public domain in the USA.

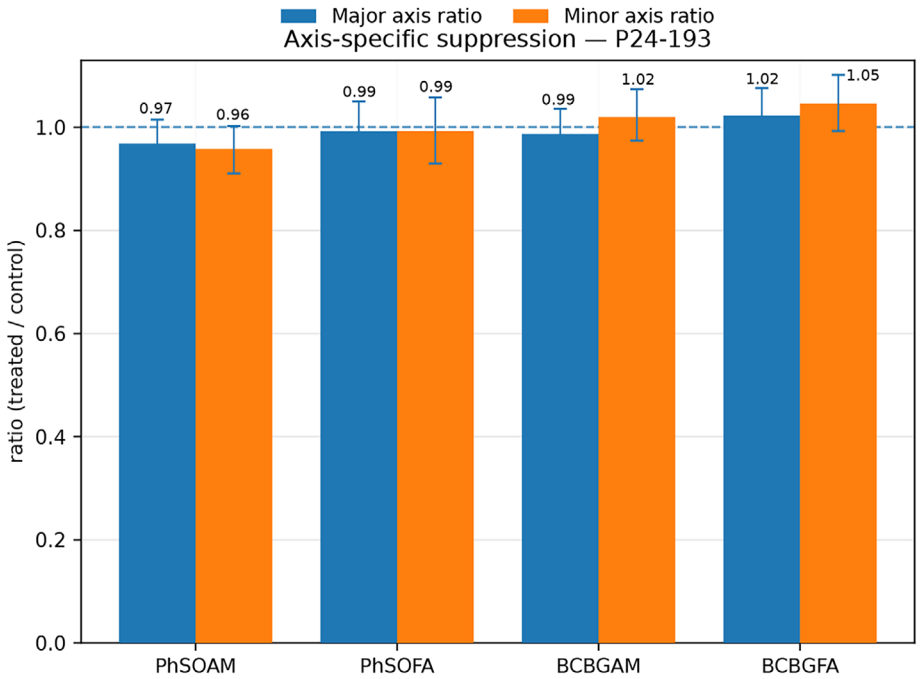

Figure 4. Axis-specific suppression (a_t/a_c, b_t/b_c). Paired bars per isolate reconstructing the major-axis (a_t/a_c) and minor-axis (b_t/b_c) ratios relative to control. These ratios are derived from area survival (S_{area}) and the LWR ratio exp (I) under the ellipse model. Ratios <1.0 indicate contraction along that axis. The representative panel for P24-193 shows bidirectional axis contraction (< 1.0) for most treatments. Analogous panels for all isolates are available in Fig. S3.

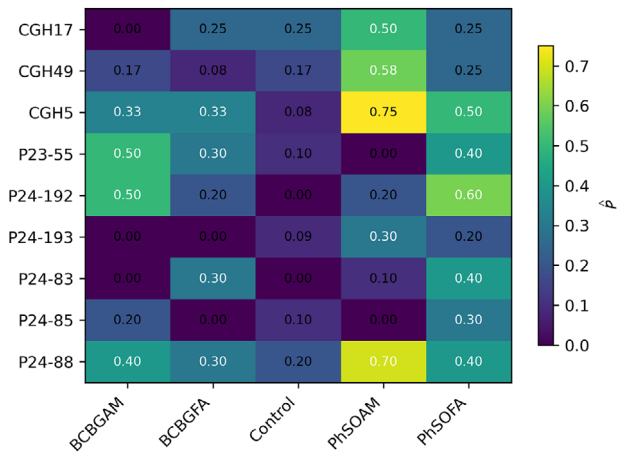

Figure 5. Event-level bounds $p(\mathbf{LWR} \geq \mathbf{1.10})$. Heatmap of the estimated probability (p) of a polarity disruption event, defined as a colony LWR ≥ 1.10. This representation converts shape disruption into a replicate-level probabilistic endpoint. Sensitivity analyses across $\tau = 1.10$–1.20 showed the expected decrease in absolute probabilities under stricter thresholds while preserving the main treatment–control contrasts for the strongest combinations (Fig. S2). Exact counts (n, k) and 95% Clopper–Pearson CIs are provided in Data S1.

asymmetry captures a real and reproducible geometric trend rather than a purely algebraic artifact.

4.3 A portable grammar for fungal stressors

Perhaps the most significant implication of this framework is its generality. Because the metrics (λ, I_{LWR}) are derived from unitless ratios, they are instrument-agnostic and pathosystem-agnostic. By extending the p-axis to an I-based event under UV-C [Fig. 3(c)], we show that the λ–I–p grammar operates coherently across chemical and physical stressors, supporting its use as a cross-modal comparative language.

This is crucial, as fungi are known to mount distinct genomic and metabolic responses to different environmental insults, such as osmotic, oxidative or chemical stress.[33,34] Our $\lambda - I$ map offers a path to capture these distinct responses as unique 'phenotypic fingerprints' captured by the λ–I–p coordinates. The λ of a chemical in this study can be directly compared to the λ of a UV-C dose or the λ of a biocontrol agent.[19] This creates a framework in which one can ask comparative questions, such as "Does *Trichoderma* exhibit a I (polarity) similar to PhSOAM?" or "What dose of UV-C achieves a similar λ (potency) as BCBGAM, and does it induce a similar I_{LWR} (polarity disruption)?" This provides a unified comparative language for image-based antifungal screening across multiple stress contexts.

4.4 Limitations and future directions

A limitation of the main chemical screen is that it was based on endpoint data from a single dose. However, we successfully demonstrated the framework's broader power on dose–response data using the external UV-C validation set (Fig. 3). This validation confirmed that both potency [$\lambda(d)$] and polarity [$I(d)$] are indeed dose-dependent. A clear future direction is to apply this dose–response approach to the chemical screening itself. Generating multidose chemical series for promising compounds (e.g. the amides) is essential. This approach, standard in pharmacokinetic/pharmacodynamic (PK/PD) modelling, would allow potency and polarity to be tracked across chemical dose series rather than inferred from a single screening dose.[35,36] A schematic illustrating how the same grammar extends to multidose chemical series is provided in Fig. S4. Likewise, the event threshold should be viewed as an operational decision rule rather than a universal

Published 2026. This article is a U.S. Government work and is in the public domain in the USA.

biological constant; in the present dataset, however, the major event-probability patterns remained interpretable across $\tau = 1.10–1.20$ (Fig. S2).

Second, time-lapse analysis is needed to validate the geometric reconstruction, testing the hypothesis that the minor axis (*b*) contracts before the major axis (*a*) under amide treatment. This is necessary to capture dynamic, nonlinear growth patterns, such as tip lysis and regeneration,[37] and is now feasible with modern image analysis toolboxes.[38]

Although λ–*I*–*p* is designed to extract mechanistic information from minimal image-derived morphology outputs, it does not by itself replace downstream physiological measurements (e.g. branching, sporulation, enzyme activity). Integrating such phenotypes is an important future direction and is naturally supported by the modular structure of the framework, but it would require additional targeted assays beyond the present dataset. Nevertheless, even with minimal morphological inputs, the framework provides high resolution: additional examples of near-equal potency (small $|\Delta\lambda|$) but divergent polarity ($|\Delta I|$) are provided in Table S1.

Finally, this phenotypic framework must be linked to its molecular drivers. Our results suggest that the amide-associated I_{LWR} signal may function as a morphological readout of perturbation in cell wall-associated processes and/or the polarized growth machinery that governs fungal morphogenesis. This interpretation is consistent with current views of the fungal cell wall as a dynamic, shape-defining structure coupled to growth direction and mechanical regulation, in which chitin- and glucan-based remodelling influences morphogenesis and stress adaptation.[39,40] In support of this general link, antifungal stress has been associated with cell wall remodelling, altered chitin/glucan balance and morphology-related tolerance responses,[39] and fungicide-induced hyphal abnormalities have been reported together with increased cell wall labelling for chitin and β-1,3-glucan.[41] We also note that related antifungal chemotypes have been linked to cell wall disruption, and the fungal cell wall remains a well-established antifungal target.[42,43] However, in the present dataset, this remains a hypothesis rather than a demonstrated molecular mechanism.

5 CONCLUSION

This study complements potency-only screening summaries by introducing a framework that integrates potency, polarity-linked geometry change, and event frequency. In the present dataset, this framework separated amide and acid chemistries in the λ–*I* plane, linked polarity shifts to axis-specific geometric contraction, and quantified replicate-level event frequencies with exact confidence bounds. By expressing colony responses in a common λ–*I*–*p* coordinate system, the approach provides a portable language for comparing image-derived antifungal responses across chemical and physical stress contexts, while remaining compatible with conventional screening workflows.

ACKNOWLEDGEMENTS

Mention of any trade names or commercial products in this article is solely for the purpose of providing specific information and does not imply recommendation or endorsement by the U. S. Department of Agriculture. USDA is an equal opportunity provider and employer, and all agency services are available without discrimination. This work was supported by the U.S. Department of Agriculture, Agricultural Research Service, In-House Projects nos 8042-21220-258-000-D and 8072-41000-113-000-D, and by the National Institute of Food and Agriculture (NIFA) under grant no. 2021-67021-34502. ChatGPT (OpenAI) was used for language editing, clarity improvement, and code refactoring during revision. The authors reviewed and verified all outputs and take full responsibility for the final manuscript.

DATA AVAILABILITY STATEMENT

Data S1 (Excel) contains the summary metrics used to generate the figures in this manuscript, including λ and *I* coordinates for each isolate–compound pair, MoA vector coordinates, axis-specific suppression ratios, event-level probabilities with exact 95% CIs across thresholds, and UV-C dose–response summaries. These tables reproduce the numerical values underlying the potency heatmaps, MOA vector fields, axis-specific suppression plots, and event-probability analyses described in the main text when the same input spreadsheets and analysis parameters are used. The analysis code is available in a public GitHub repository (https://github.com/EJSAHN/lambda-I-p-analysis). Input datasets are available from the cited sources; the repository does not redistribute raw datasets.

AUTHOR CONTRIBUTIONS

Ezekiel Ahn: Writing – original draft, Supervision, Project administration, Methodology, Formal analysis, Data curation, Conceptualization. Insuck Baek: Writing – review & editing, Validation, Software, Formal analysis. Seunghyun Lim: Writing – review & editing, Formal analysis. Amelia Lovelace: Writing – review & editing, Resources. Kazem-Rostami: Resources, Methodology. Helen Ngo: Writing – review & editing, Validation, Resources. Richard D. Ashby: Writing – review & editing, Validation, Resources. Minhyeok Cha: Writing – review & editing, Resources. Moon S. Kim: Writing – review & editing, Supervision, Resources, Funding acquisition. Sunchung Park: Writing – review & editing, Methodology. Lyndel W. Meinhardt: Writing – review & editing, Supervision, Resources, Funding acquisition.

SUPPORTING INFORMATION

Supporting information may be found in the online version of this article.

REFERENCES

1 Reyes G and Ghannoum MA, Antifungal susceptibility testing of yeasts: uses and limitations. *Drug Resist Updat* **3**:14–19 (2000).
2 Beattie SR and Krysan DJ, Antifungal drug screening: thinking outside the box to identify novel antifungal scaffolds. *Curr Opin Microbiol* **57**: 1–6 (2020).
3 Noel ZA, Wang J and Chilvers MI, Significant influence of EC50 estimation by model choice and EC50 type. *Plant Dis* **102**:708–714 (2018).
4 Hadacek F and Greger H, Testing of antifungal natural products: methodologies, comparability of results and assay choice. *Phytochem Anal Int J Plant Chem Biochem Technol* **11**:137–147 (2000).
5 Li J, Liu X, Xie J, Di Y and Zhu F, A comparison of different estimation methods for fungicide EC50 and EC95 values. *J Phytopathol* **163**: 239–244 (2015).
6 Badawy ME, Rabea EI and Abdelgaleil SA, Studies on the EC50 of natural monoterpenes as fungal inhibitors with quantitative structure-activity relationships (QSARs). *Nat Prod J* **10**:44–60 (2020).
7 Barry D and Williams G, Microscopic characterisation of filamentous microbes: towards fully automated morphological quantification through image analysis. *J Microsc* **244**:1–20 (2011).

Published 2026. This article is a U.S. Government work and is in the public domain in the USA.

8 Goriely A and Tabor M, Mathematical modeling of hyphal tip growth. *Fungal Biol Rev* **22**:77–83 (2008).
9 Bowman SM and Free SJ, The structure and synthesis of the fungal cell wall. *Bioessays* **28**:799–808 (2006).
10 Berepiki A, Lichius A and Read ND, Actin organization and dynamics in filamentous fungi. *Nat Rev Microbiol* **9**:876–887 (2011).
11 O'Meara TR, Veri AO, Ketela T, Jiang B, Roemer T and Cowen LE, Global analysis of fungal morphology exposes mechanisms of host cell escape. *Nat Commun* **6**:6741 (2015).
12 Beattie SR and Krysan DJ, A unique dual-readout high-throughput screening assay to identify antifungal compounds with aspergillus fumigatus. *Msphere* **6**:10–1128 (2021).
13 Sabburg R, Gregson A, Urquhart AS, Aitken EA, Smith L, Thatcher LF *et al.*, A method for high-throughput image-based antifungal screening. *J Microbiol Methods* **190**:106342 (2021).
14 Ohnuki S, Ogawa I, Itto-Nakama K, Lu F, Ranjan A, Kabbage M *et al.*, High-throughput platform for yeast morphological profiling predicts the targets of bioactive compounds. *Npj Syst Biol Appl* **8**:3 (2022).
15 Clopper CJ and Pearson ES, The use of confidence or fiducial limits illustrated in the case of the binomial. *Biometrika* **26**:404–413 (1934).
16 Owen WJ, Yao C, Myung K, Kemmitt G, Leader A, Meyer KG *et al.*, Biological characterization of fenpicoxamid, a new fungicide with utility in cereals and other crops. *Pest Manag Sci* **73**:2005–2016 (2017).
17 Baek I, Jang JH, Lim S, Wang Z, Cha M, Magill C *et al.*, Differential responses of Cacao pathogens Colletotrichum gloeosporioides and Pestalotiopsis sp. to UVB 305 nm and UVC 275 nm. *Sci Rep* **15**: 1–18 (2025).
18 Pfendler S, Karimi B, Alaoui-Sosse L, Bousta F, Alaoui-Sossé B, Abdel-Daim MM *et al.*, Assessment of fungi proliferation and diversity in cultural heritage: reactions to UV-C treatment. *Sci Total Environ* **647**:905–913 (2019).
19 Baek I, Bhatt J, Jang JH, Lim S, Lovelace A, Cha M *et al.*, Dissecting Trichoderma antagonism: role of strain identity, volatiles, biomass, and morphology in suppressing cacao pathogens. *Biol Control* **207**: 105807 (2025).
20 Narayanasamy P, Mechanisms of action of fungal biological control agents, Biological management of diseases of crops: Volume 1: Characteristics of biological control agents, Springer, pp. 99–200 (2013).
21 McKinney W, Data structures for statistical computing in Python. *scipy* **445**:51–56 (2010).
22 Harris CR, Millman KJ, Van Der Walt SJ, Gommers R, Virtanen P, Cournapeau D *et al.*, Array programming with NumPy. *Nature* **585**: 357–362 (2020).
23 Virtanen P, Gommers R, Oliphant TE, Haberland M, Reddy T, Cournapeau D *et al.*, SciPy 1.0: fundamental algorithms for scientific computing in python. *Nat Methods* **17**:261–272 (2020).
24 Ahn E, Kazem-Rostami M, Park S, Ashby R, Ngo H and Meinhardt L, Quantitative morphological profiling and isolate-specific insensitivity of cacao pathogens to novel bio-based phenolic amides. *J Fungi* **33**: 12 (2026).
25 Baek I, Lim S, Lovelace A, Oh S, Kazem-Rostami M, Ngo H *et al.*, Taxonomy-agnostic hyperspectral–morphological phenotyping of fungal pathogen chemical-stress responses using machine learning. *Smart Agric Technol* **13**:101895 (2026).
26 Huang K, Fan X, Ashby R and Ngo H, Structure-activity relationship of antibacterial bio-based epoxy polymers made from phenolic branched fatty acids. *Prog Org Coat* **155**:106228 (2021).
27 Kazem-Rostami M, Ryu V, Wagner K, Jones K, Mullen CA, Wyatt V *et al.*, Antibacterial agents from waste grease: arylation of Brown grease fatty acids with beechwood creosote and derivatization. *ACS Sustain Chem Eng* **11**:17760–17768 (2023).
28 Ngo H, Wagner K, Cermak S, Fan X, Kazem-Rostami M, Sarker MI *et al.*, Branched-chain fatty acids based on biomass fast pyrolysis Phenolics. *Eur J Lipid Sci Technol* **127**:e70002 (2025).
29 Ahn E, Baek I, Lim S, Lovelace A, Cha M, Kim MS *et al.*, From minutes to bounds: A probabilistic UV-C control and a shape-only morphological fingerprint for postharvest Colletotrichum inactivation in cacao and coffee processing. *Food Control* 111956 (2026).
30 Ōmura S, Katagiri M, Awaya J, Furukawa T, Umezawa I, Ōi N *et al.*, Relationship between the structures of fatty acid amide derivatives and their antimicrobial activities. *Antimicrob Agents Chemother* **6**:207–215 (1974).
31 Heleno SA, Martins A, Queiroz MJR and Ferreira IC, Bioactivity of phenolic acids: metabolites versus parent compounds: a review. *Food Chem* **173**:501–513 (2015).
32 Patra S, Banerjee S, Terejanu G and Chanda A, Subsurface pressure profiling: a novel mathematical paradigm for computing colony pressures on substrate during fungal infections. *Sci Rep* **5**:12928 (2015).
33 Gasch AP, Comparative genomics of the environmental stress response in ascomycete fungi. *Yeast* **24**:961–976 (2007).
34 Jacobsen MD, Beynon RJ, Gethings LA, Claydon AJ, Langridge JI, Vissers JP *et al.*, Specificity of the osmotic stress response in Candida albicans highlighted by quantitative proteomics. *Sci Rep* **8**:14492 (2018).
35 Lewis RE, Liao G, Hou J, Prince RA and Kontoyiannis DP, Comparative in vivo dose-dependent activity of caspofungin and anidulafungin against echinocandin-susceptible and-resistant Aspergillus fumigatus. *J Antimicrob Chemother* **66**:1324–1331 (2011).
36 Siopi M, Siafakas N, Vourli S, Mouton JW, Zerva L and Meletiadis J, Dose optimization of voriconazole/anidulafungin combination against Aspergillus fumigatus using an in vitro pharmacokinetic/pharmacodynamic model and response surface analysis: clinical implications for azole-resistant aspergillosis. *J Antimicrob Chemother* **71**:3135–3147 (2016).
37 Moreno-Velásquez SD, Seidel C, Juvvadi PR, Steinbach WJ and Read ND, Caspofungin-mediated growth inhibition and paradoxical growth in Aspergillus fumigatus involve fungicidal hyphal tip lysis coupled with regenerative intrahyphal growth and dynamic changes in β-1, 3-glucan synthase localization. *Antimicrob Agents Chemother* **61**:10–1128 (2017).
38 Brunk M, Sputh S, Doose S, van de Linde S and Terpitz U, HyphaTracker: an ImageJ toolbox for time-resolved analysis of spore germination in filamentous fungi. *Sci Rep* **8**:605 (2018).
39 Lima SL, Colombo AL and de Almeida Junior JN, Fungal cell wall: emerging antifungals and drug resistance. *Front Microbiol* **10**:2573 (2019).
40 Gow NA and Lenardon MD, Architecture of the dynamic fungal cell wall. *Nat Rev Microbiol* **21**:248–259 (2023).
41 Kang Z, Huang L, Krieg U, Mauler-Machnik A and Buchenauer H, Effects of tebuconazole on morphology, structure, cell wall components and trichothecene production of fusarium culmorum in vitro. *Pest Manag Sci Former Pestic Sci* **57**:491–500 (2001).
42 Ni T, Xie F, Li L, Hao Y, Chi X, Yan L *et al.*, Design, synthesis and structure-activity relationship studies of nicotinamide derivatives as potent antifungal agents by disrupting cell wall. *Molecules* **28**:1135 (2023).
43 Liu W, Yuan L and Wang S, Recent progress in the discovery of antifungal agents targeting the cell wall. *J Med Chem* **63**:12429–12459 (2020).

Published 2026. This article is a U.S. Government work and is in the public domain in the USA.